An EmrB multidrug efflux pump in *Burkholderia thailandensis* with unexpected roles in antibiotic resistance

Received for publication, November 8, 2018, and in revised form, December 12, 2018 Published, Papers in Press, December 13, 2018, DOI 10.1074/jbc.RA118.006638

Afsana Sabrin, Brennan W. Gioe, Ashish Gupta[1], and Anne Grove[2]

From the Department of Biological Sciences, Louisiana State University, Baton Rouge, Louisiana 70803

Edited by Chris Whitfield

The antibiotic trimethoprim is frequently used to manage *Burkholderia* infections, and members of the resistance-nodulation-division (RND) family of efflux pumps have been implicated in multidrug resistance of this species complex. We show here that a member of the distinct *Escherichia coli* multidrug resistance B (EmrB) family is a primary exporter of trimethoprim in *Burkholderia thailandensis*, as evidenced by increased trimethoprim sensitivity after inactivation of *emrB*, the gene that encodes EmrB. We also found that the *emrB* gene is up-regulated following the addition of gentamicin and that this up-regulation is due to repression of the gene encoding OstR, a member of the multiple antibiotic resistance regulator (MarR) family. The addition of the oxidants H_2O_2 and $CuCl_2$ to *B. thailandensis* cultures resulted in OstR-dependent differential *emrB* expression, as determined by qRT-PCR analysis. Specifically, OstR functions as a rheostat that optimizes *emrB* expression under oxidizing conditions, and it senses oxidants by a unique mechanism involving two vicinal cysteines and one distant cysteine (Cys^3, Cys^4, and Cys^{169}) per monomer. Paradoxically, *emrB* inactivation increased resistance of *B. thailandensis* to tetracycline, a phenomenon that correlated with up-regulation of an RND efflux pump. These observations highlight the intricate mechanisms by which expression of genes that encode efflux pumps is optimized depending on cellular concentrations of antibiotics and oxidants.

Bacteria experience diverse environmental challenges during host infection. To survive, they must withstand host-derived stresses, such as changes in temperature, pH, generation of reactive oxygen species (ROS),[3] and nutrient scarcity. In addition, they may encounter antibiotics, disinfectants, and other harmful chemicals. To proliferate in the face of such challenges, bacteria employ diverse transcription factors, which respond to the environmental changes and modulate gene expression. Multiple antibiotic resistance regulator (MarR) family transcriptional regulators often participate in regulating expression of virulence genes in response to environmental cues (1). First characterized in *Escherichia coli* K-12, MarR was shown to play critical roles in conferring resistance to antibiotics, household disinfectants, and oxidative stress (2). Members of the protein family named for *E. coli* MarR are ubiquitous in bacterial species, and the most common mode of transcriptional regulation involves binding to the intergenic DNA between the gene encoding the MarR homolog and divergently or adjacently oriented genes, thereby hindering access of RNA polymerase to the promoter. DNA binding by a given MarR family protein may be modified upon binding to small-molecule ligands or oxidants, a result of which is altered expression of genes in its regulon (1).

Many pathogenic *Burkholderia* species exhibit inherent resistance to a wide range of antibiotics and disinfectants (3). Efflux systems involved in antibiotic resistance include the resistance-nodulation-division (RND) efflux systems and the *E. coli* multidrug resistance B (EmrB) family transporters (3–5). Extensively studied pathogens include *Burkholderia pseudomallei*, a soil saprophyte causing melioidosis, and its clonal derivative *Burkholderia mallei*, a host-adapted pathogen, which is the causative agent of glanders (6). Both are categorized as category B priority pathogens because of the low infectious dose, capability for aerosol transmission, and resistance to antibiotics (3). By contrast, *Burkholderia cenocepacia* is an opportunistic pathogen that primarily infects immunocompromised patients (7). *Burkholderia thailandensis* is particularly closely related to *B. pseudomallei* and *B. mallei*, and these species are founding members of the *B. pseudomallei* (Bpc) group (8, 9). *B. thailandensis* is much less virulent despite conservation of many genes involved in virulence (10).

One of the very early host responses to a bacterial infection is the production of ROS. For example, NADPH oxidase generates superoxide radicals ($O_2^{\bullet-}$), which give rise to H_2O_2. H_2O_2 may in turn oxidize ferrous iron to generate highly reactive hydroxyl radicals ($OH^{\bullet}$) (11, 12). ROS can target bacterial DNA, protein, or membrane lipids and thus can attenuate bacterial survival and proliferation in the host environment (13). Transition metals, such as Cu(II) and Zn(II), can also cause microbial poisoning when in excess (14). In addition, Cu(II) can participate in the Fenton reaction and cause elevated intracellular ROS production.

This work was supported by National Science Foundation Grant MCB-1714219 (to A. Grove) and by a donation from P. Campbell in support of undergraduate research. The authors declare that they have no conflicts of interest with the contents of this article.
This article contains Tables S1–S4.

[1] Present address: Novavax, Inc., Process Development Dept., Gaithersburg, MD 20878.
[2] To whom correspondence should be addressed: Dept. of Biological Sciences, Louisiana State University, Baton Rouge, LA 70803. Tel.: 225-578-5148; E-mail: agrove@lsu.edu.

[3] The abbreviations used are: ROS, reactive oxygen species; EmrB, *E. coli* multidrug resistance B; EMSA, electrophoretic mobility shift assay; MarR, multiple antibiotic resistance regulator; MIC, minimal inhibitory concentration; OstR, oxidant-sensing transport regulator; RND, resistance-nodulation-division; PAR, 4-(2-pyridylazo) resorcinol; LB, lysogeny broth; LSLB, low-salt LB; qPCR, quantitative PCR.

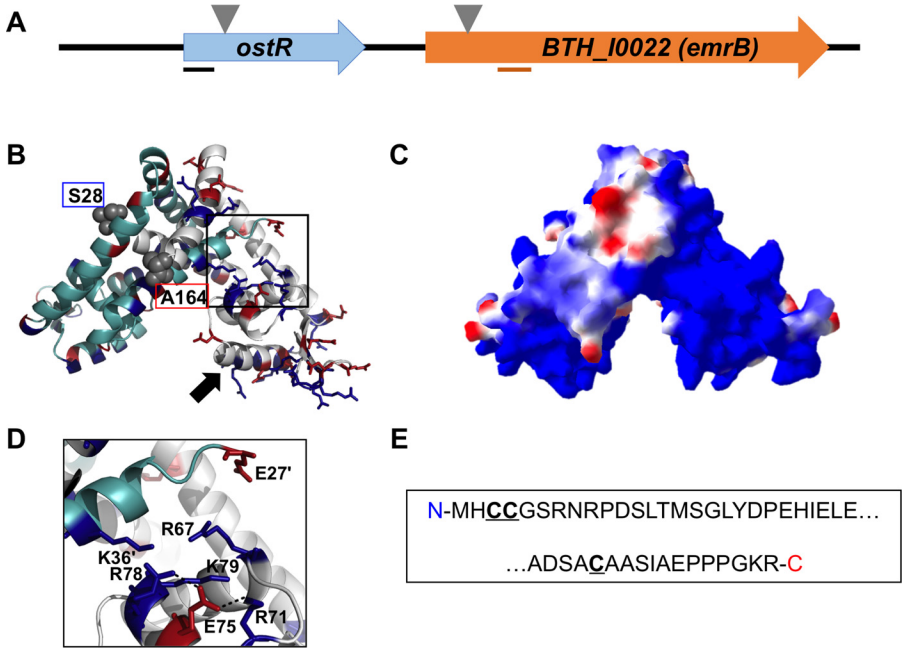

Figure 1. *Burkholderia thailandensis* OstR. *A*, *ostR-emrB* genomic locus. Transposon insertion is indicated by *inverted triangles*. *Lines below* the *arrows* illustrating open reading frames represent the positions of PCR amplicons used for quantitative RT-PCR. *B*, predicted model of OstR based on template 4AIK, created by SwissModel (in automated mode; GMQE 0.55) and visualized by PyMOL. One monomer is shown in *cyan* and the other is in *gray*, with positively charged residues in *blue* and negatively charged amino acids in *red*. Serine at position 28 and alanine at position 164 (marking the range of amino acids included in the model) are shown in *space-filling representation*. *Black arrow*, DNA recognition helix. *C*, electrostatic surface potential was calculated using Swiss PDB Viewer (*red*, negative; *blue*, positive). *D*, *magnified image* of the positively charged patch. *E*, N- and C-terminal extensions of OstR that are not included in the modeled structure, with cysteines in *boldface type* and *underlined*.

Bacterial responses to ROS by transcriptional regulators such as MarR family proteins have been described, including in *Burkholderia* species (15, 16); oxidation of cysteine residues, usually by reversible formation of disulfide linkages, leads to conformational changes that allow such transcriptional regulators to promote expression of genes involved in detoxification of ROS or repair of ROS-mediated damage (17). The redox-active Cu(II) has also been implicated in modification of MarR proteins by inducing formation of disulfide linkages between separate dimers, but with distinct outcomes (15, 18).

B. thailandensis encodes 12 annotated MarR homologs, all of which are conserved in *B. pseudomallei* and *B. mallei* (19). One of these is encoded by *BTH_I0021*, which is upstream of a gene encoding an EmrB/QacA family transport protein. This genomic locus is conserved among pathogenic species such as *B. pseudomallei*, *B. mallei*, and *B. cenocepacia* (19). Based on the identified roles of this MarR family protein in oxidant sensing and control of a transporter, we have assigned the name OstR (oxidant-sensing transport regulator). We report here differential and OstR-dependent expression of *BTH_I0022* encoding the EmrB family transporter under reducing and oxidizing conditions and that OstR employs a novel response to oxidants involving vicinal cysteines. Notably, disruption of *BTH_I0022* confers sensitivity to trimethoprim, an antibiotic commonly used in combination with sulfamethoxazole to treat *Burkholderia* infections. Unexpectedly, disruption of *BTH_I0022* also confers increased resistance to tetracycline, a resistance that correlates with up-regulation of an RND efflux pump.

Results

Conserved genomic locus encoding OstR and EmrB

The gene encoding OstR is immediately upstream of *BTH_I0022*, which encodes an EmrB/QacA family drug resistance transporter (Fig. 1*A*). A model of OstR was predicted using SwissModel and 4AIK (*Yersinia pseudotuberculosis* RovA (20)) as a template, one of the structures with highest sequence identity to OstR (28%). This model shows the expected homodimer, which consists of a dimerization region formed by N- and C-terminal α1, α5, and α6 helices from both subunits and a DNA-binding region that includes recognition helices α4/α4′ (*arrow*; Fig. 1*B*). In addition, each monomer contains N- and C-terminal extensions beyond the conserved core fold that is represented in the modeled structure, with the core fold spanning residues Ser^{28}–Ala^{164} (Fig. 1*B*; terminal residues in *gray space-filling representation*). The electrostatic surface potential of the OstR core was calculated by Swiss PDB Viewer. Notably, one lobe of the dimeric protein is predicted to be highly positively charged (Fig. 1*C*). The other lobe features a more usual distribution of charges, being electropositive surrounding the recognition helix and the wing regions, a common feature that would promote interaction with the negatively charged cognate DNA. The unusual surface charge distribution within one protein lobe appears to derive from a constellation of five Arg and Lys residues, which is not balanced by equivalent negative charge (Fig. 1*D*); salt bridges between Glu^{75} and Arg^{71}/Arg^{78} are predicted, whereas the side chain of $Glu^{27\prime}$ is predicted to be >8 Å from the other positively charged side chains ($Lys^{36\prime}$, Arg^{67}, and Lys^{79}). Another notable feature of the OstR

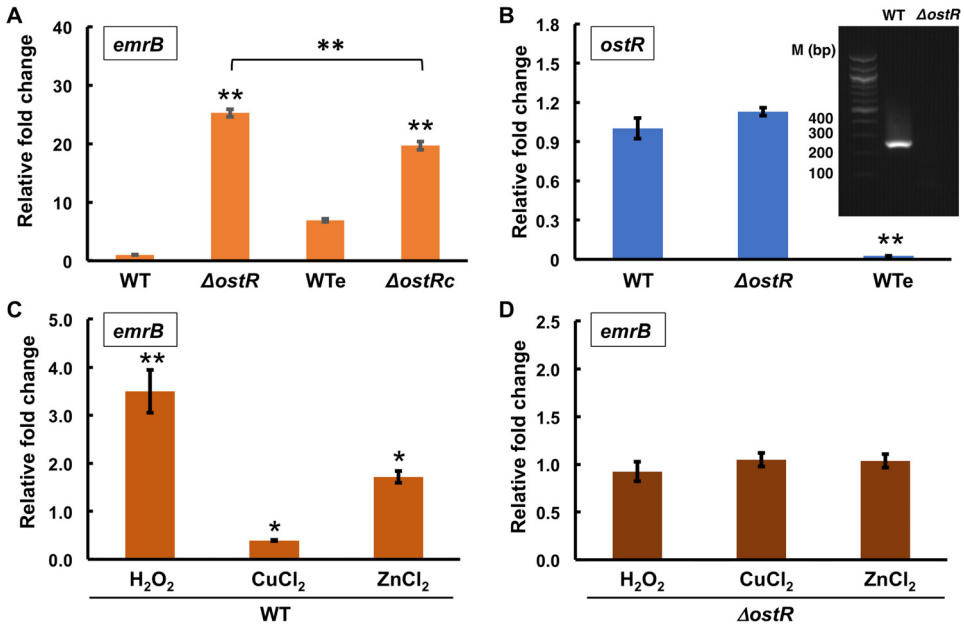

Figure 2. Regulation of gene expression. *A*, relative transcript level of *emrB* in WT, Δ*ostR*, WTe (containing empty vector), and Δ*ostR*c (complemented with *ostR*) strains. -Fold changes are reported relative to the reference gene encoding glutamate synthase large subunit (*BTH_I3014/BTH_RS27550*) and normalized to expression in WT cells, except for expression in Δ*ostR*c, which is reported relative to WTe. *Error bars*, S.D. values of three biological replicates. *B*, relative -fold change in transcript level of *ostR* in Δ*ostR* strain calculated by the $2^{-\Delta CT}$ method relative to the reference gene and normalized to expression in WT cells. The gel shows expression of *ostR* in WT and Δ*ostR* strains. *Lane 1*, 100-bp DNA marker. *C* and *D*, relative abundance of transcript level of the gene encoding EmrB in the presence of 2 mM H_2O_2, $CuCl_2$, and $ZnCl_2$ in WT and Δ*ostR* strains. The transcript levels were calculated using $2^{-\Delta\Delta CT}$ relative to the reference gene and normalized to expression in the corresponding unsupplemented cultures. *Error bars*, S.D. of three individual experiments. *Asterisks* represent statistically significant differences in expression compared with WT cells, except as indicated in *A*, based on a Student's *t* test (*, $p < 0.05$; **, $p < 0.001$).

sequence is the presence of three cysteine residues per monomer, two vicinal cysteines (Cys^3 and Cys^4) in the N-terminal extension that precedes the core MarR fold and Cys^{169} in the C-terminal extension (Fig. 1*E*). With six cysteines per dimer, regulation of OstR function by oxidation would be possible.

OstR regulates emrB differentially in response to oxidants

To assess whether OstR participates in regulation of *emrB*, we obtained and verified *B. thailandensis* E264 mutant strains in which *ostR* or *emrB* genes were disrupted by the insertion of transposons at position 98 of *ostR* and position 89 of *emrB* open reading frames, respectively, to generate Δ*ostR* and Δ*emrB* strains (Fig. 1*A*) (21). Relative transcript levels of *emrB* were measured in both WT and Δ*ostR* strains. *emrB* was up-regulated 25.2 ± 0.7-fold in the Δ*ostR* strain (Fig. 2*A*), suggesting that OstR is a repressor of *emrB*. Complementation of Δ*ostR* was attempted using plasmid-encoded *ostR*. Because a gentamicin-resistant derivative of the broad host range vector pBBR1-MCS5 was used for this purpose, WT cells were transformed with empty pBBR1-MCS5 (generating strain WTe) to control for any effects of gentamicin on gene expression. However, restoration of WT levels of *emrB* expression was not achieved in Δ*ostR* transformed with pBBR1-MCS5-*ostR* (Δ*ostR*c) and grown with gentamicin, only an ~20% reduction in expression compared with WTe. To address the possible reason, expression of *ostR* was determined in WTe grown with gentamicin and found to be significantly reduced (Fig. 2*B*). Consistent with a gentamicin-mediated reduction in *ostR* expression, *emrB* expression was ~7-fold higher in WTe compared with WT cells (Fig. 2*A*). This suggests that gentamicin negatively regulates the expression of *ostR*, a consequence of which is increased *emrB* expression.

Many MarRs are autoregulatory (1). To determine whether any autoregulation of *ostR* by OstR occurs, we analyzed expression of the gene fragment that is upstream of the point of transposon insertion (position 98 of the *ostR* ORF). There was no significant difference in expression between WT and Δ*ostR*, indicating that expression of *ostR* is not regulated by OstR (Fig. 2*B*). By contrast, analysis of *ostR* expression using primers, which amplify a fragment that is downstream of the transposon insertion, showed no expression in Δ*ostR* consistent with transposon-mediated gene disruption (Fig. 2*B*, *gel inset*); combined with the ~25-fold increase in *emrB* expression in Δ*ostR*, this experiment also shows that *emrB* is expressed under the control of its own promoter.

To determine the effect of oxidants on the expression of *emrB*, WT and Δ*ostR* strains were grown to mid-log phase followed by incubation with a 2 mM concentration of the oxidant H_2O_2 or $CuCl_2$ for 30 min. RNA was isolated, and cDNA was made using gene-specific primers for analysis of relative transcript levels by quantitative RT-PCR. In the presence of 2 mM H_2O_2, *emrB* expression was increased 3.5 ± 0.4-fold, whereas incubation with 2 mM $CuCl_2$ resulted in significant reduction in *emrB* expression (0.4 ± 0.01-fold; Fig. 2*C*). To determine whether redox-inactive metals also regulate *emrB* expression, we assessed Zn^{2+}-dependent transcriptional regulation of *emrB*. Gene expression analysis revealed an ~2-fold increase in *emrB* expression in the presence of 2 mM $ZnCl_2$. No significant change in *emrB* expression was observed in the Δ*ostR* strain in the presence of oxidants or $ZnCl_2$, suggesting that the observed

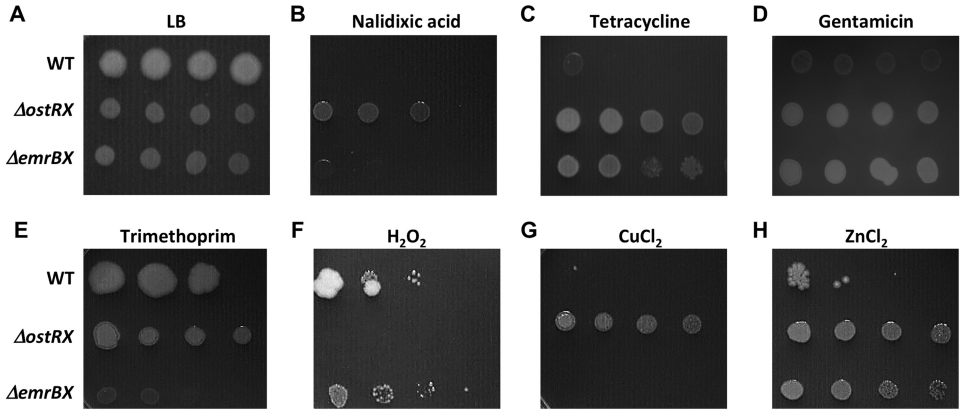

Figure 3. Gene deletions alter resistance to antibiotics and oxidants. In each *panel*, the *top row* shows WT, the *middle row* shows Δ*ostRX*, and the *bottom row* shows Δ*emrBX* (strains deleted for antibiotic resistance cassettes within transposons). Spots represent 10-fold serial dilutions of the indicated strains; the doubling time of mutant strains (~60 min) is greater than that of WT cells (~26 min). *A*, LB. *B*, nalidixic acid (10 μg/ml). *C*, tetracycline (1 μg/ml). *D*, gentamicin (150 μg/ml). *E*, trimethoprim (50 μg/ml). *F*, treatment with 5 mM H_2O_2. *G*, 5 mM $CuCl_2$. *H*, 2 mM $ZnCl_2$.

changes in gene expression in WT cells depend on OstR (Fig. 2*D*).

Gene disruption affects sensitivity to antibiotics and oxidants

For clues to the substrate for EmrB, the WT, Δ*ostRX*, and Δ*emrBX* strains (in which antibiotic resistance cassettes were removed from transposons) were serially diluted and spotted on LB-agar plates containing antibiotics. It was previously reported that expression of the corresponding *B. cepacia* EmrB protein (named BcrA) in *E. coli* resulted in resistance to tetracycline and nalidixic acid (22). Nalidixic acid was seen to be toxic to WT cells and to Δ*emrBX*, whereas the Δ*ostRX* strain was more resistant (Fig. 3*B*). A minimal inhibitory concentration (MIC) was estimated by growing the respective strains in liquid culture containing serially diluted antibiotics; this analysis indicated a similar MIC for WT and Δ*emrBX* cells, whereas the MIC *for* Δ*ostRX* cells was higher (Table 1). The increased resistance exhibited by Δ*ostRX* would be consistent with upregulation of *emrB* and more efficient export of nalidixic acid.

Resistance to tetracycline was likewise elevated in the Δ*ostRX* strain, consistent with export through EmrB; however, resistance was also increased in the Δ*emrBX* strain (Fig. 3*C* and Table 1). Expression of two operons encoding RND efflux systems (BpeEF-OprC and AmrAB-OprA) was previously reported to be induced by the tetracycline derivative doxycycline (23); a possible explanation for the increased resistance to tetracycline in the Δ*emrBX* strain is therefore that failure to export tetracycline through EmrB might lead to elevated intracellular concentrations and induction of one or both of these RND efflux systems. We therefore grew Δ*emrBX* and Δ*ostRX* strains in the presence of different concentrations of tetracycline and measured expression of *amrB* and *bpeF* (Fig. 4). Expression of *amrB* was greater in Δ*emrBX* cells grown with at least 10 μg/ml tetracycline, whereas expression of *bpeF* was reduced. In contrast, expression of both *amrB* and *bpeF* was reduced in Δ*ostRX* cells grown with tetracycline. This is consistent with the inference that the increased resistance to tetracycline characteristic of Δ*emrBX* cells is due to induction of the operon that encodes AmrAB-OprA.

High concentrations of gentamicin were tolerated by WT cells, with a further increase in resistance in Δ*ostRX* cells (Fig. 3*D* and Table 1). Because increased resistance was also observed in Δ*emrBX* cells, one possibility is that failure to export gentamicin by EmrB may result in induction of an alternate exporter, as seen for tetracycline. Notably, EmrB appears to be a primary efflux system for trimethoprim; at a concentration of the antibiotic where growth of WT and Δ*ostRX* was largely unaffected, as estimated by plate assays, growth of Δ*emrBX* was severely compromised (Fig. 3*E*). Consistent with EmrB being important for trimethoprim efflux, the MIC for Δ*emrBX* cells was lower than the MIC for WT cells (Table 1).

Table 1
MIC in LB medium

B. thailandensis E264 derivative	Concentration			
	Nalidixic acid	Tetracycline	Gentamicin	Trimethoprim
			μg/ml	
WT	64	2	2,000	64
Δ*ostRX*	256	8	32,000	>1,000
Δ*emrBX*	64	4	16,000	16

Because *emrB* expression was sensitive to redox state (Fig. 2*C*), the strains were exposed to either 5 mM H_2O_2 or $CuCl_2$ and plated on LB-agar plates. Whereas the Δ*emrBX* strain exhibited similar sensitivity to either oxidant as WT cells, Δ*ostRX* was more sensitive to H_2O_2 but less sensitive to $CuCl_2$ (Fig. 3, *F* and *G*). This differential sensitivity is intriguing, and it parallels the opposite effects of either oxidant on *emrB* expression, suggesting that gene regulation by oxidized OstR depends on the identity of the oxidant. Exposure to $ZnCl_2$, however, resulted in a phenotype similar to that observed on treatment with tetracycline and gentamicin (Fig. 3*H*).

Interaction of OstR with Zn^{2+} and oxidants in vitro

OstR was examined *in vitro*, focusing on responses to the inducers of differential *emrB* expression *in vivo*. The gene encoding OstR was cloned, and the protein was expressed in *E. coli* and purified using a nickel-nitrilotriacetic acid–agarose column to apparent homogeneity (Fig. 5 (*E* and *F*), *lanes 2*). The calculated molecular mass of monomeric OstR is ~21 kDa. Far-UV CD spectroscopy showed that the predicted secondary structure composition of OstR is about 37% α-helix, 25%

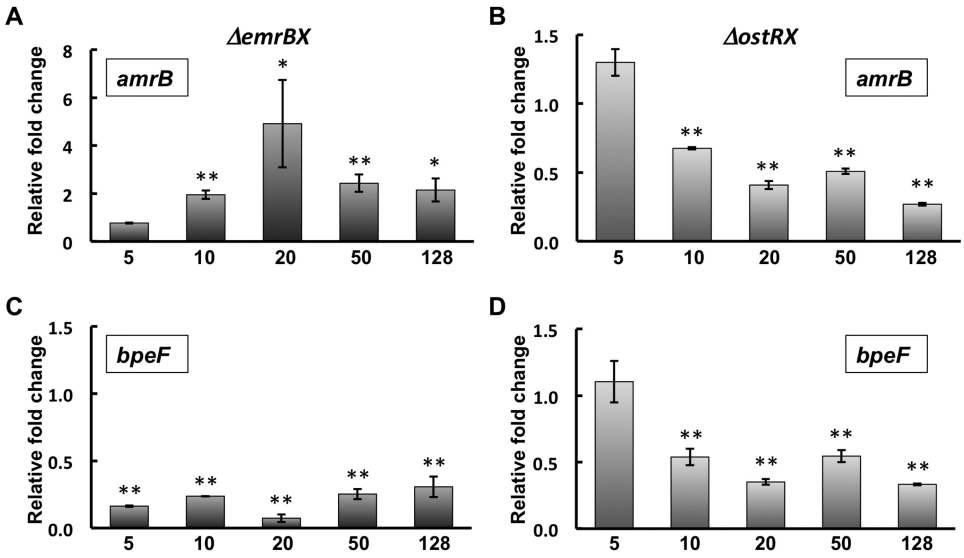

Figure 4. Expression of genes encoding AmrAB-OprA and BpeEF-OprC efflux pumps in the presence of tetracycline. *A* and *B*, expression of *amrB* (*BTH_I2444*) in Δ*emrBX* and Δ*ostRX*, respectively. *C* and *D*, expression of *bpeF* (*BTH_II2105*) in Δ*emrBX* and Δ*ostRX*, respectively. Expression is reported relative to unsupplemented cultures. *Asterisks* represent statistically significant differences in expression compared with unsupplemented cultures based on Student's *t* test (*, $p < 0.05$; **, $p < 0.001$). *Horizontal axes* identify the concentration of tetracycline (in μg/ml). Note that the *ordinate scale* for *A* differs from that in *B–D*. *Error bars*, S.D.

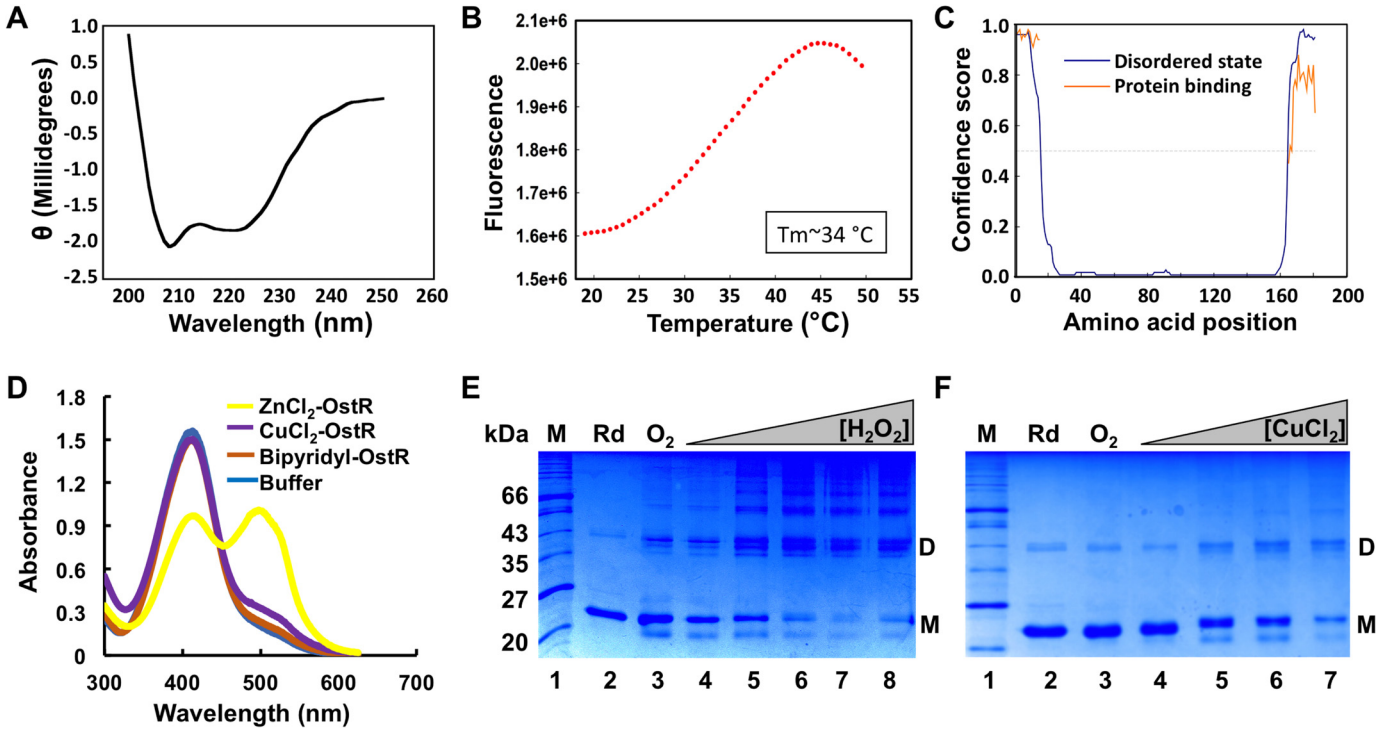

Figure 5. Characterization of OstR. *A*, far-UV CD spectrum of OstR. Ellipticity is presented in machine units (millidegrees). *B*, thermal denaturation of OstR determined by differential scanning fluorometry. Fluorescence intensity reflects binding of SYPRO Orange to hydrophobic regions of denatured protein as a function of temperature. *C*, prediction of intrinsically disordered regions (*blue*) and likelihood of disordered regions participating in protein interactions (*orange*). The *y* axis reflects confidence score, with values >0.5 considered relevant. *D*, release of metal ion from denatured OstR determined by absorbance of PAR. Absorbance at 416 nm corresponds to uncomplexed PAR, whereas absorbance at 520 nm reflects formation of PAR–metal ion complex. *E* and *F*, OstR oxidation by H_2O_2 (*E*) and $CuCl_2$ (*F*). In both images, the *left lanes* show protein marker (kDa), *lanes 2* show protein incubated with DTT (*Rd*; species migrating at ~43 kDa is residual oxidized protein), and *lanes 3* show air-oxidized protein (O_2). *E*, *lanes 4–8*, increasing concentration of H_2O_2 (10 μM to 2 mM). *F*, *lanes 4–7*, increasing concentration of $CuCl_2$ (10 μM to 2 mM).

β-sheet, and 38% random coils (Fig. 5*A*). By comparison, the structure of *Deinococcus radiodurans* HucR, which also has an N-terminal extension beyond the conventional MarR fold, reveals ~55% α-helix, a helical content that is also reflected in its CD spectrum; the lower α-helical content for OstR may reflect that its unique N- and C-terminal extensions are not helical (24, 25). The secondary structure of OstR was predicted using the PSIPRED Protein Analysis Workbench (26); disorder prediction using DISOPRED3 revealed that the extensions beyond the core MarR fold represent intrinsically disordered

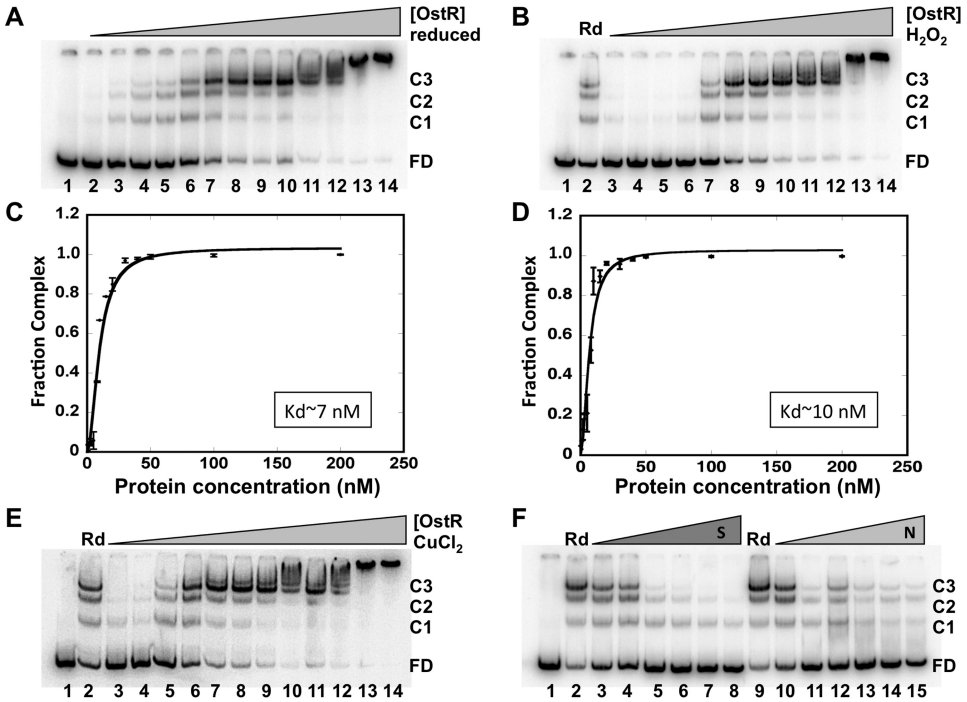

Figure 6. OstR binds *emrB* promoter DNA. *A*, EMSA showing reduced OstR binding *emrB* promoter DNA (0.2 nM). DNA was titrated with increasing concentration of OstR (1–200 nM; *lanes 2–14*). *Lane 1*, free DNA only. Free DNA and protein–DNA complex are shown as *FD* and *C1–C3*, respectively, at the *right*. *B* and *E*, EMSA showing oxidized OstR binding *emrB* promoter DNA. Reactions in *lanes 1* contained free DNA only, and reactions in *lanes 2* contained reduced OstR. *Lanes 3–14*, operator DNA (0.2 nM) titrated with increasing concentration (1–200 nM) of oxidized protein (oxidized with 2 mM H_2O_2 and 5 μM $CuCl_2$, respectively). Normalized complex fraction for reduced OstR (*C*) and normalized complex fraction for H_2O_2-oxidized OstR (*D*) are plotted as a function of OstR concentration. S.D. values of three replicates are represented as *error bars*. *F*, EMSA showing OstR (5 nM) bound to 0.2 nM labeled operator DNA challenged with increasing concentration of specific unlabeled 146-bp operator DNA (0.2–50 nM, *lanes 3–8*) or nonspecific DNA pET28b (0.2–10 nM, *lanes 10–15*). The reaction in *lane 1* contained free DNA only; the reactions in *lanes 2* and *9* contained no competitor DNA.

regions and that they likely participate in protein interaction, both with high confidence scores (Fig. 5*C*).

A thermal stability assay in which SYPRO Orange was used as a fluorescent reporter of protein unfolding as a function of temperature showed that reduced OstR exhibited a one-step melting transition with a relatively low $T_m = 34.1 \pm 0.1$ °C (Fig. 5*B*). Protein stability was found to increase in the presence of DNA ($T_m = 39.3 \pm 0.2$ °C) and Zn^{2+} ($T_m = 37.2 \pm 0.1$ °C) or upon oxidation ($T_m \sim 39$ °C; Table S1). Incubation of OstR with bipyridyl prior to measurement of thermal stability did not affect the T_m, indicating that purified OstR had no metal ions already bound. To verify binding to metal ions, OstR was incubated with 2 mM $ZnCl_2$ followed by treatment with 4-(2-pyridylazo) resorcinol (PAR). The metallochromic indicator PAR chelates zinc ions released from the protein upon its denaturation, which results in an absorbance peak at ~520 nm, whereas uncomplexed PAR has an absorbance maximum at 416 nm (27). As shown by the marked absorbance at 520 nm, OstR binds Zn^{2+} (Fig. 5*D*).

Each OstR monomer harbors three cysteine residues, all within the N- and C-terminal extensions (Fig. 1*E*). Reduced OstR was therefore incubated with increasing concentration of H_2O_2 and $CuCl_2$, and oxidation products were analyzed by electrophoresis on SDS-polyacrylamide gels. When oxidized with H_2O_2, OstR formed dimers and oligomeric species as well as intramolecular disulfide bonds, as indicated by a species with a faster migration than reduced monomeric protein. In addition, OstR formed three dimeric forms with distinct mobility, likely reflecting different disulfide-bonded species (Fig. 5*E*).

OstR was also oxidized by $CuCl_2$. Whereas the appearance of multiple dimeric species was more evident on H_2O_2-mediated oxidation, intramolecular disulfide bonds and oligomeric species were also seen upon oxidation with $CuCl_2$.

OstR binds the emrB promoter

Electrophoretic mobility shift assays (EMSAs) were performed to determine OstR binding upstream of *emrB*. Reduced OstR bound the 146-bp DNA spanning *ostR* and *emrB* forming multiple complexes (Fig. 6*A*). The apparent dissociation constant K_d was 6.7 ± 0.8 nM with Hill coefficient $n_H = 1.9 \pm 0.3$, indicating positive cooperativity of binding (Table S2 and Fig. 6*C*). At lower protein concentration, the faster-migrating complex C1 was visible, whereas the slower-migrating complex C3 remained predominant across a greater range of concentration. Nonspecific binding may occur at even higher protein concentration, leading to slower migration of the complexes. To address whether OstR bound specifically to the *emrB* promoter, increasing concentration of competitor DNA was added in the reaction with specific labeled DNA and a constant concentration of the protein. Specific unlabeled DNA competed efficiently for OstR binding (Fig. 6*F*, *lanes 3–8*). Nonspecific DNA did not compete as efficiently for OstR binding to its cognate DNA (Fig. 6*F*, *lanes 10–15*; note that the highest concentration of specific competitor DNA represents a 250-fold excess over specific labeled DNA, whereas the highest concentration of the 5,368-bp pET28b represents an almost 2,000-fold excess).

OstR was oxidized with 2 mM H_2O_2, and DNA binding was visualized by EMSA (Fig. 6, *B* and *D*). The affinity of H_2O_2-

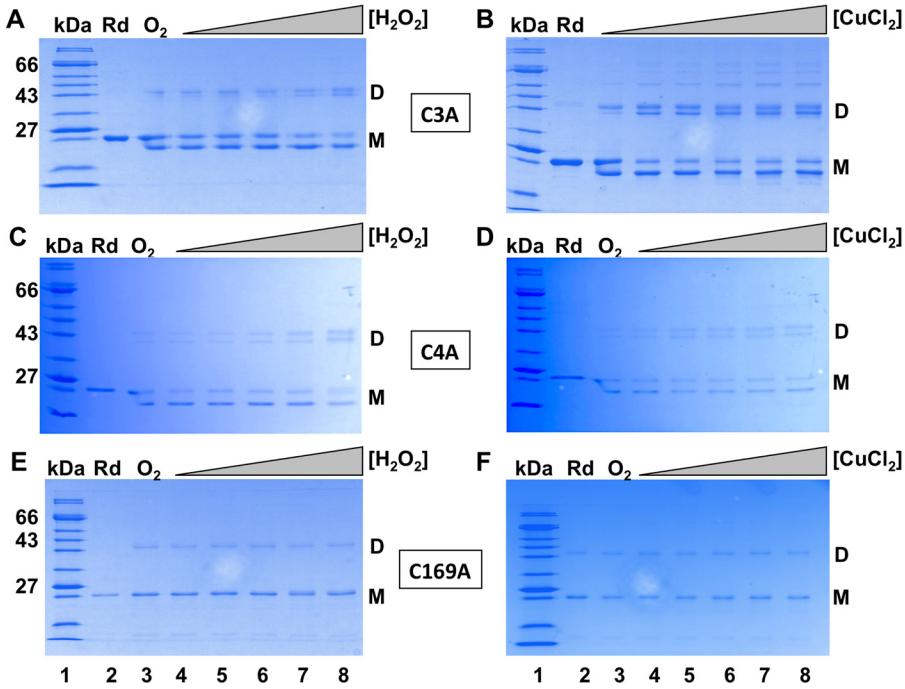

Figure 7. Oxidation of OstR cysteine variants by H_2O_2 and $CuCl_2$. *A*, *C*, and *E*, OstR-C3A. OstR-C4A and OstR-C169A oxidized with increasing concentration of H_2O_2 (10 μM to 2 mM). *B*, *D*, and *F*, OstR-C3A. OstR-C4A and OstR-C169A oxidized with increasing concentration of $CuCl_2$ (10 μM to 2 mM). *Lanes 1*, protein marker (kDa); *lanes 2*, reduced protein (*Rd*); *lanes 3*, air-oxidized protein (O_2), except for *B*, in which air-oxidized protein is not shown.

oxidized OstR for cognate DNA was not markedly different from that of reduced protein (K_d = 9.7 ± 1.1). Incubation of increasing concentration of 2 mM $CuCl_2$-oxidized OstR with *emrB* promoter DNA also showed no significant change in DNA-binding affinity, K_d = 6.5 ± 1.0 (Fig. 6*E* and Table S2).

Substitution of cysteine residues leads to altered binding affinity for promoter DNA

To determine the role of cysteines in oxidant sensing by OstR, we replaced each cysteine with alanine and created three individual cysteine mutants (OstR-C3A, OstR-C4A, and OstR-C169A). Each variant was expressed in *E. coli* and purified to apparent homogeneity (Fig. 7, *lanes 2*). The yield of OstR-C169A mutant was lower compared with the other variants, with precipitation observed after purification, indicating that the absence of Cys^{169} may cause instability or improper folding.

Increasing concentrations of OstR-C3A, OstR-C4A, or OstR-C169A were incubated with 146-bp *emrB* promoter DNA followed by analysis of protein–DNA complexes by EMSA (Fig. 8, *A*, *C*, and *E*). OstR-C3A showed a modest reduction in DNA-binding affinity with K_d = 17.5 ± 2.3 and Hill coefficient, n_H = 1.6 ± 0.3 (Fig. 8*B*). OstR-C4A exhibited a comparable reduction in DNA-binding affinity with K_d = 23.4 ± 3.2 and n_H = 1.2 ± 0.3 (Fig. 8*D*). Replacing Cys^{169} with alanine, however, caused DNA binding to be significantly impaired, with K_d = 539 ± 58 nM and n_H = 1.9 ± 0.2 (Fig. 8*E* and Table S2). Because the cysteine residues all reside in extensions beyond the core MarR fold, these data suggest that modulation of these extensions leads to structural rearrangements that impact the DNA-binding region, an impact that implies an interaction between the extensions and the protein core.

Cys^{169} participates in intramolecular disulfide bond formation

The role of individual cysteines in disulfide bond formation was investigated by incubation of OstR variants with increasing concentration of H_2O_2 (Fig. 7, *A*, *C*, and *E*) or $CuCl_2$ (Fig. 7, *B*, *D*, and *E*), followed by analysis by SDS-PAGE. All variants were readily oxidized on exposure to air (*lanes 3*). Intramolecular disulfide bonds were seen for both OstR-C3A and OstR-C4A, as evidenced by a product that migrated faster than reduced, monomeric OstR (Fig. 7, *A–D*). By contrast, such faster-migrating monomeric species were absent with oxidized OstR-C169A (Fig. 7, *E* and *F*), suggesting that Cys^{169} is required for intramolecular disulfide bond formation. Oxidized OstR-C3A and OstR-C4A also formed two prominent dimeric species, whereas oxidized WT OstR featured three dimeric species and oxidized OstR-C169A formed only one. Higher-order oligomeric species were observed in the presence of $CuCl_2$, but not in the case of H_2O_2-mediated oxidation.

All cysteines play a structural role

Differential scanning fluorometry showed that OstR-C3A and OstR-C4A are thermally more stable (T_m = 44.7 ± 0.1 and 50.6 ± 0.1 °C, respectively) than WT OstR (Fig. 9*A* (*red dotted line*) and Fig. 7*B* (*blue dotted line*), respectively). The addition of oxidants (H_2O_2 or $CuCl_2$), however, resulted in significant destabilization of these mutant variants, as reflected in high initial fluorescence and the absence of a melting transition (Fig. 9, *A* (*blue dashed line*) and *B* (*purple dashed line*), respectively, and Table S3). Upon binding to ligands such as DNA or zinc, both OstR-C3A and OstR-C4A variants showed significant increase in thermal stability

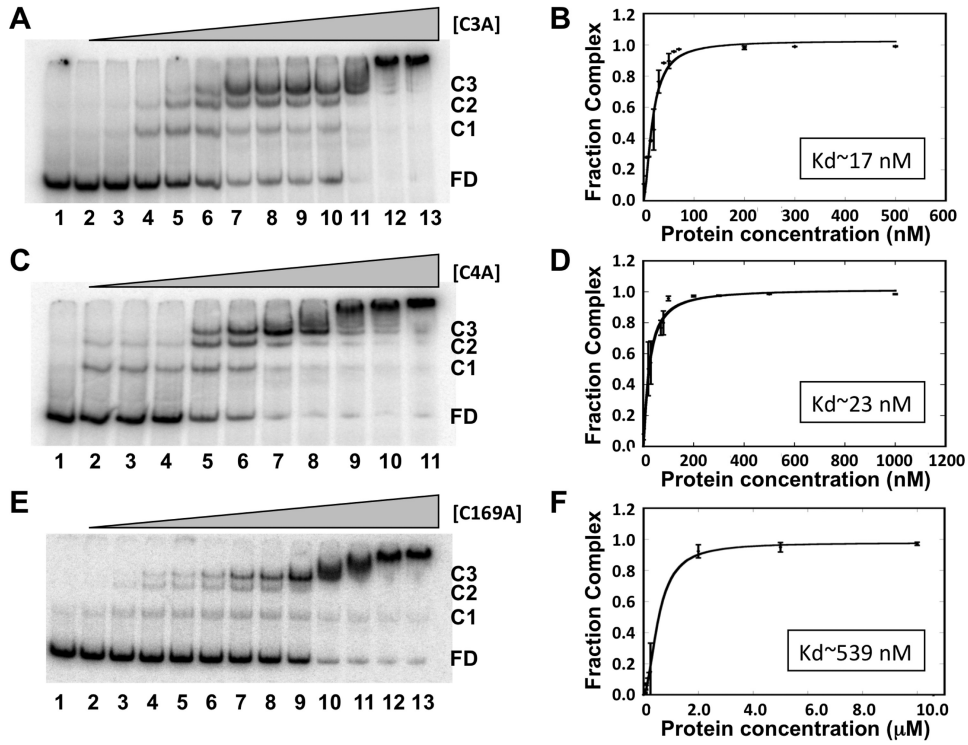

Figure 8. Cysteine variants bind DNA with reduced affinity. *A*, OstR-C3A binding *emrB* promoter DNA. DNA (0.2 nM) was titrated with increasing concentration of OstR-C3A (1–200 nM; *lanes 2–13*). *Lane 1*, free DNA only. Free DNA and protein–DNA complex are shown as *FD* and *C1–C3*, respectively, at the *right*. *C* and *E*, EMSA showing binding of OstR-C4 and OstR-C169A to promoter DNA, respectively. *B*, *D*, *F*, normalized complex fraction for OstR-C3A, OstR-C4A, and OstR-C169A, respectively, plotted as a function of protein concentration. *Error bars*, S.D. of three replicates.

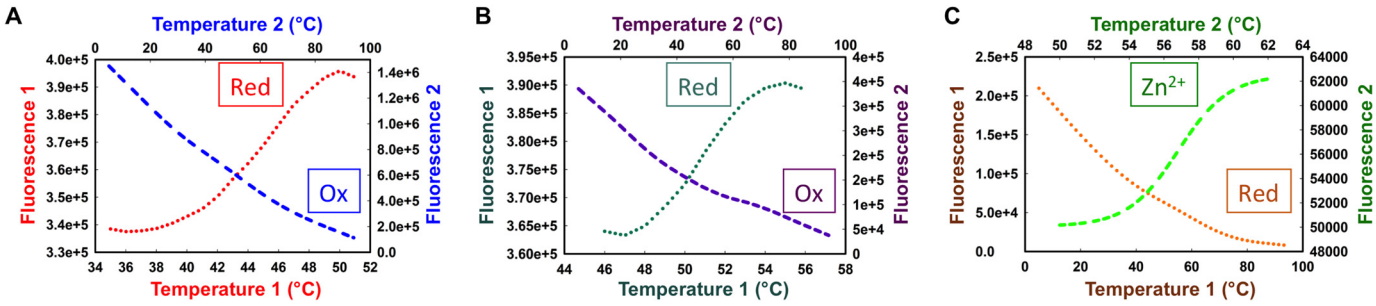

Figure 9. Differential scanning fluorometry showing thermal stability of cysteine variants. Fluorescence intensity reflects binding of SYPRO Orange to hydrophobic regions of denatured protein as a function of temperature. *A*, reduced OstR-C3A (*red dotted line*; *left* and *bottom axes*) and H_2O_2 oxidized OstR-C3A (*blue dashed line*; *right* and *top axes*). *B*, reduced OstR-C4A (*teal dotted line*; *left* and *bottom axes*) and H_2O_2-oxidized OstR-C4A (*purple dashed line*; *right* and *top axes*). *C*, reduced OstR-C169A (*orange dotted line*; *left* and *bottom axes*) and OstR-C169A bound to Zn^{2+} (*green dashed line*; *right* and *top axes*).

(Table S3). By contrast, OstR-C169A exhibited a high initial fluorescence and a decrement in fluorescence as a function of temperature and no identifiable melting transition (Fig. 9*C*, *orange dotted line*). Such a pattern of interaction with SYPRO Orange suggests that OstR-C169A exposes hydrophobic residues, indicating improper folding and a feature reminiscent of molten globule formation. The addition of oxidant had no effect on this pattern. In the presence of zinc, OstR-C169A behaved as a globular protein with a clear melting transition (Fig. 9*C*, *green dashed line*). Incubation of OstR-C169A with DNA also resulted in protein stabilization (Table S3), consistent with the ability of this protein variant to bind DNA (albeit with low affinity; Fig. 8 (*E* and *F*)). That substitution of either cysteine impacted thermal stability is consistent with the inference that both N- and C-terminal extensions contact the protein core.

All three cysteine variants bind to zinc

The Zn^{2+}-mediated changes in thermal stability of OstR cysteine variants suggested metal binding. All OstR variants were incubated with 2 mM $ZnCl_2$, followed by denaturation and measurement of released Zn^{2+} by chelation to PAR. Significant absorbance peaks at ~520 nm were observed for all three variants, indicating release of Zn^{2+} from denatured proteins (Fig. 10, *A–C*). This suggests that none of the three cysteines were required to coordinate Zn^{2+} in OstR. Based on this information, we opted to assess whether Zn(II) binding modulated cysteine oxidation *in vitro*. The OstR variants were incubated with 2 mM $ZnCl_2$ for 30 min, followed by oxidation with 12 mM H_2O_2 for another 30 min. SDS-PAGE analysis showed that both OstR-C3A and OstR-C4A formed intramolecular disulfide bonds, dimeric species, and higher-order oligomers

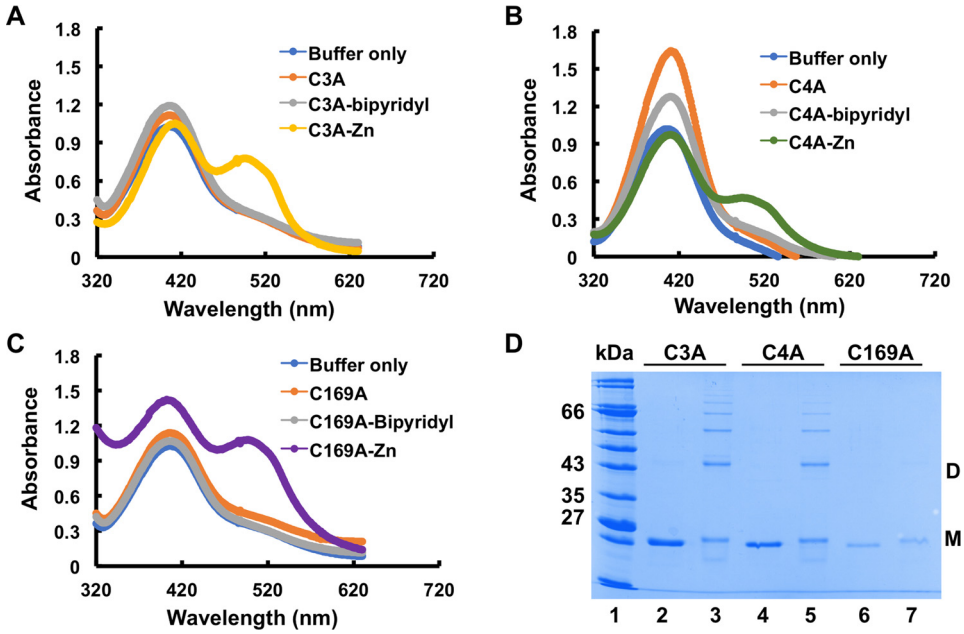

Figure 10. All cysteine variants bind Zn^{2+}. *A–C*, release of Zn^{2+} from denatured OstR-C3A, OstR-C4A, and OstR-C169A, respectively, determined by absorbance of Zn^{2+} in complex with PAR (peak absorbance at 520 nm). *D*, identified cysteine mutants were incubated with 2 mM $ZnCl_2$ for 30 min followed by treatment with 12 mM H_2O_2 for another 30 min (*lanes 3*, *5*, and *7*). *Lanes 2*, *4*, and *6*, Zn^{2+}-treated OstR-C3A, OstR-C4A, and OstR-C169A, respectively.

(Fig. 10*D*, *lanes 3* and *5*, respectively). The OstR-C169A variant also formed dimers (faint dimeric species in Fig. 10*D*, *lane 7*) upon oxidation, but due to the presence of both metal and oxidant, the protein precipitated significantly. That Zn^{2+} did not preclude cysteine oxidation is consistent with the interpretation that neither Cys^3, Cys^4, nor Cys^{169} is required for Zn^{2+} coordination.

Discussion

Antibiotic efflux by EmrB

Trimethoprim inhibits dihydrofolate reductase, and it is frequently used in combination with sulfamethoxazole (as co-trimoxazole) to treat *Burkholderia* infections. In *B. pseudomallei*, the RND efflux pump BpeEF-OprC has been shown to extrude trimethoprim (28). Our data identify the EmrB drug transporter encoded by *BTH_I0022* as another primary transporter of trimethoprim, as evidenced by the increased sensitivity imposed by its inactivation (Fig. 3*E* and Table 1).

Expression of the *B. cepacia* EmrB ortholog (BcrA) in *E. coli* resulted in increased resistance to nalidixic acid and tetracycline (trimethoprim was not tested) (22). The *emrB* expression is increased in the Δ*ostRX* strain that shows enhanced resistance to both nalidixic acid and tetracycline (Fig. 3 (*B* and *C*) and Table 1), consistent with facilitated efflux. However, we cannot rule out that genes encoding other drug transporters are up-regulated as a result of inactivation of *ostR*, thereby conferring or contributing to the observed resistance. Because inactivation of the *emrB* gene did not result in increased sensitivity to nalidixic acid, we also infer that other mechanisms for efflux of this compound exist.

By contrast, the increased resistance to tetracycline in the Δ*emrBX* strain points to a more intricate cross-talk between efflux systems. The tetracycline derivative doxycycline was previously shown to induce expression of two RND efflux systems, AmrAB-OprA at intermediate concentrations of doxycycline, followed by BpeEF-OprC at very high drug concentrations (23). It was also noted that the addition of an RND inhibitor resulted in a 2–3-fold increase in expression of *amrB*, an overexpression that was associated with elevated resistance to certain antibiotics. Consistent with these observations, we find that *amrB* expression is induced in Δ*emrBX* cells grown with tetracycline, an induction that does not occur in Δ*ostRX* cells. This is consistent with the interpretation that failure to export tetracycline through EmrB leads to induction of *amrB* (Fig. 4). Taken together, these observations point to a complex mechanism for induction of optimal efflux systems, which should be considered when attempting to restore multidrug resistance by controlling activity of specific efflux pumps.

Redox-dependent differential regulation of emrB by OstR

OstR represses expression of *emrB* and modulates its expression under conditions of oxidative stress (Fig. 2). Preferred binding of OstR to the *emrB* promoter is consistent with the observed regulation. Reduced and H_2O_2-oxidized OstR bind to *emrB* promoter DNA with comparable affinity (Fig. 6, *A–D*), yet the presence of oxidant affects gene expression (Fig. 2*C*). Changes in gene expression due to features other than altered DNA-binding affinity of the cognate transcription factor have been reported previously. For example, the redox-sensitive MarR homolog HypR in *Bacillus subtilis* binds to DNA with similar affinity regardless of redox state, but only oxidized HypR activates target gene expression (29). Similarly, PecS from the plant pathogen *Pectobacterium atrosepticum* binds to promoter DNA with comparable affinity at pH 7.4 and 8.3, but it represses gene expression only at alkaline pH; in the case of PecS, the differential ability to repress gene activity was ascribed to its pH-dependent ability to alter DNA topology (30). Reduced and oxidized OstR may likewise impose distinct con-

formational changes in promoter DNA that manifest as differential ability to compete with RNA polymerase for binding.

OstR also senses Cu^{2+}, which results in further repression of *emrB* (Fig. 2*C*). The opposite effects of H_2O_2 and Cu^{2+} suggest that the different oxidants result in different OstR oxidation products and therefore distinct effects on gene expression; such opposite effects also manifest in the distinct changes in sensitivity to these oxidants imposed by deletion of *ostR*, consistent with differential control of genes in the OstR regulon (Fig. 3, *F* and *G*). Reduced and Cu^{2+}-oxidized OstR also bind to promoter DNA with equivalent affinity (Table S2). By comparison, the *B. thailandensis* MarR homolog BifR, which is also subject to Cu^{2+}-mediated oxidation, forms a dimer of dimers when oxidized and acts as a "superrepressor" to attenuate gene expression further even though oxidation has little effect on DNA-binding affinity (15). Taken together, our data suggest that reduced OstR represses *emrB* and that it operates as a rheostat in the presence of oxidants to optimize *emrB* expression.

Modification of cysteines affects stability of OstR

Oxidation of OstR and the Cys-to-Ala mutants results in formation of dimeric species (Figs. 5 (*E* and *F*) and 7). As evidenced by the formation of an oxidized species that migrates faster than reduced, monomeric OstR, we also infer that Cys^{169} can participate in intramolecular disulfide linkages with either Cys^3 or Cys^4 (Fig. 7). The presence of three dimeric species upon oxidation of WT protein (two dimeric species with OstR-C3A and OstR-C4A and one dimer with oxidized OstR-C169A) could be explained by the formation of intermolecular disulfide bonds involving either Cys^3 or Cys^4 from two OstR dimers alone (as seen for OstR-C169A) or in combination with intramolecular disulfide linkages between Cys^{169} and either Cys^3 or Cys^4, resulting in oxidized species with distinct mobilities.

Differential scanning fluorometry reveals that OstR-C169A exposes hydrophobic residues (Fig. 9*C*), suggesting that it is intrinsically unfolded or that it exists in a molten globule state (25); considering that a closely packed protein conformation with a distinct melting transition is restored in the presence of Zn^{2+} or DNA, we speculate that it may be the latter. By contrast, OstR-C3A and OstR-C4A mutants are thermally more stable compared with WT OstR (Tables S1 and S3). That thermal stability is altered as a result of either mutation indicates that neither N- nor C-terminal extensions are disordered; rather, they are docked to the core fold of the protein (consistent with the prediction for participation in protein interaction; Fig. 5*C*).

Notably, oxidation of both OstR-C3A and OstR-C4A leads to a fluorescence profile similar to that observed for reduced OstR-C169A, indicating disruption of the protein fold (Fig. 9, *A* and *B*). The unusual electrostatic surface potential that characterizes one lobe of OstR in which positively charged residues are predicted to be clustered (Fig. 1, *C* and *D*) affords a clue to the observed destabilization of cysteine mutants. We propose that the C-terminal extension interacts with this positive patch and that a thiolate anion of Cys^{169} is required to neutralize excess positive charges; electrostatic interactions that stabilize the thiolate anion would lower the pK_a of cysteine compared with its intrinsic pK_a of ~8.5 (31). In the absence of Cys^{169}, electrostatic repulsion would result in a disruption of the compact protein fold. This model also explains the need for the vicinal cysteines in the N-terminal extension and the observed destabilization that occurs on oxidation of OstR-C3A and OstR-C4A; upon formation of an intramolecular disulfide bridge between either Cys^3 or Cys^4 and Cys^{169}, the Cys^{169} thiolate is lost. Protein stability, therefore, requires the thiolate form of the neighboring N-terminal cysteine, rationalizing why oxidation of an OstR variant with only one N-terminal cysteine would lead to a loss of the protein fold.

The addition of $ZnCl_2$ increases thermal stability of WT OstR and all cysteine variants (Tables S1 and S3), and the PAR assay supports the conclusion that OstR binds Zn^{2+} (Figs. 5*D* and 10 (*A–C*)). Because Zn^{2+}-binding restores a compact fold to OstR-C169A, one possibility is that it coordinates residue(s) in the N-terminal extension and near the positively charged patch (Fig. 1, *D* and *E*), thereby promoting association of the N-terminal vicinal cysteines (which are preceded by His) with the positively charged patch, supplying a required negative charge.

Taken together, our data identify *B. thailandensis* OstR as a novel oxidant-sensitive regulator of the downstream gene encoding an EmrB family transporter. Its unique N- and C-terminal extensions contact the core fold of the protein, in the process modulating protein stability and responses to oxidants. Substrates for EmrB include commonly used antibiotics; whereas inactivation of *emrB* leads to trimethoprim sensitivity, it results in markedly increased resistance to tetracycline, a resistance that correlates with induced expression of the RND efflux pump AmrAB-OprA, illustrating the intricate mechanisms by which expression of genes encoding efflux pumps is optimized depending on cellular concentrations of inducing antibiotic.

Experimental procedures

Protein modeling and purification

PyMOL was used to visualize the model of OstR, which was generated by homology modeling using SwissModel in automated mode and Protein Data Bank entry 4AIK as template (selected as allowing the most residues of OstR to be included in the model).

The gene encoding *B. thailandensis* E264 OstR was amplified from genomic DNA using primers OstR_tran_Fw and OstR_tran_Rv containing NdeI and EcoRI restriction sites, respectively (Table S4). The PCR product was cloned into pET28b after restriction digestion with NdeI and EcoRI to express N-terminal His_6-tagged protein. The construct was verified by sequencing and then transformed into *E. coli* BL21(DE3). Cells were grown until mid-exponential phase at 37 °C in LB with 50 μg/ml kanamycin, followed by induction using 1 mM isopropyl β-D-1-thiogalactopyranoside. After 1 h, cells were pelleted at 4 °C and stored at −80 °C. Cell pellets were thawed, and cells were resuspended in wash buffer (50 mM sodium phosphate (pH 7.0), 250 mM NaCl, 5% glycerol). Lysozyme (final concentration 1 mg/ml) and 2 μl of DNase I with 50 μl of 10× DNase I reaction buffer were added to each 5-ml cell suspension, which was incubated at 4 °C for 60 min.

Lysate was obtained by centrifugation at 10,000 × *g* for 1 h at 4 °C and incubated with 1 ml of HIS-Select nickel affinity beads (previously washed with two volumes of distilled H_2O and one volume of wash buffer) at 4 °C for 1 h. The beads were then transferred to a gravity flow column to elute protein by the addition of increasing concentrations of imidazole (10–200 mM). Pure protein fractions were detected by SDS-PAGE, pooled, and concentrated using Amicon centrifugal filter units (Millipore). Protein was dialyzed overnight against 50 mM sodium phosphate (pH 7.0), 250 mM NaCl, 10% glycerol, and 5 mM 2-mercaptoethanol. Concentrations were determined based on the absorbance at 280 nM, using a calculated extinction coefficient of 7,450 M^{-1} cm^{-1}. To create cysteine-to-alanine substitutions, overhanging primers (Table S4) were used to amplify the whole plasmid harboring the *ostR* gene, reactions were incubated with DpnI, and the DNA was transformed into *E. coli* TOP10 (Invitrogen); plasmids were sequenced for verification. Mutant proteins were purified as described above.

To determine secondary structure of the protein, the far-UV CD spectrum was measured using a Jasco J-815 CD spectrophotometer (32). In brief, 0.2 mg/ml protein in CD buffer (20 mM sodium phosphate (pH 7.0), 20 mM NaCl, 0.8% glycerol, and 1.5 mM DTT) was used to measure ellipticity. A quartz cuvette with 0.1-cm path length was used after equilibrating protein the sample at room temperature. The K2D program from Dichroweb was used to calculate secondary structure of the protein (33–35). The fitness of data was determined by the normalized root mean square deviation value at a range of 0.094 – 0.110.

To determine oligomeric states upon oxidation, WT protein and cysteine mutants were treated with increasing concentration of the oxidants (H_2O_2 and $CuCl_2$) on ice for 20 min followed by termination of the reaction by adding Laemmli sample buffer without 2-mercaptoethanol. Samples were analyzed by SDS-PAGE after heating at 90 °C for 8 min, followed by staining with Coomassie Brilliant Blue.

DNA binding

To determine protein–DNA interaction, an EMSA was performed. Increasing concentration of OstR was incubated on ice for 30 min with 146-bp *ostR-emrB* intergenic DNA amplified from *B. thailandensis* E264 genomic DNA with primers BTH_22int_Fw and BTH_22int_Rv (Table S4) and 5′-end–labeled using [γ-^{32}P]ATP and T4 polynucleotide kinase. Protein and DNA were mixed in binding buffer containing 20 mM Tris-HCl (pH 8.0), 50 mM NaCl, 0.1 mM EDTA, and 0.1 mM DTT. Pre-run 8% polyacrylamide gels were used to separate free DNA and protein–DNA complex, followed by phosphorimaging using a Typhoon PhosphorImager (GE Healthcare). Densitometric data were quantified by ImageQuant version 5.1 and are presented based on an average of three replicates ± S.D. KaleidaGraph version 4.0 (Synergy Software) was used to calculate the equilibrium dissociation constant (K_d) by fitting the data to the equation, $f_{max} \times (P^{nH}/K_d)/(1 + P^{nH}/K_d{}^{nH})$, where f_{max} is maximal saturation, P is OstR concentration, and n_H is the Hill coefficient. EMSA was performed also at 37 °C.

To determine the effect of oxidants on protein–DNA binding, increasing concentrations of oxidized OstR (previously oxidized with 2 mM H_2O_2 or 5 μM $CuCl_2$) were incubated with *intergenic* DNA, and EMSAs were performed as described above. To assess the specificity of DNA binding, protein and labeled DNA was titrated with increasing concentrations of unlabeled specific 146-bp operator DNA or with nonspecific unlabeled DNA (pET28b), followed by EMSA.

Thermal stability assay

3 μM protein was added to thermal stability assay buffer (50 mM Tris (pH 8.0), 50 mM NaCl) along with SYPRO Orange (5×). Increasing temperature from 5 to 94 °C (in 1 °C increments) was used in an Applied Biosystems 7500 real-time PCR system for protein unfolding, which was measured by fluorescence of SYPRO Orange bound to the hydrophobic core of denatured protein. Corrected fluorescence emission was obtained by subtracting control values. SigmaPlot version 9 was used for determination of melting temperature by regression analysis using a four-parameter sigmoidal equation. The T_m was calculated from the averages of three technical replicates obtained from each of three independent experiments and is presented as mean ± S.D.

Metal binding

Proteins were incubated with 50 mM 2,2′-bipyridyl at 4 °C to remove any bound metals. Bipyridyl-treated proteins were dialyzed overnight against buffer A (50 mM Tris-HCl (pH 8.0), 250 mM NaCl, 2 mM 2-mercaptoethanol, and 10% glycerol) and then incubated with 1 mM $ZnCl_2$ on ice for 30 min and again dialyzed overnight against buffer A to remove unbound metal. Proteins were denatured by adding 1% SDS in assay buffer (20 mM Tris-HCl (pH 7.5), 50 mM sodium chloride) followed by heating at 90 °C for 10 min. 100 μM PAR was added to each sample and buffer control, and an Agilent 8453 spectrophotometer was used to measure absorbance from 320 to 630 nm. Fluorescence data are reported as the mean of three technical replicates from representative experiments.

Confirmation of transposon mutants and removal of antibiotic resistance cassettes

ostR (*BTH_I0021*) and *emrB* (*BTH_I0022*) were disrupted by the insertion of transposon T8 at position 98 of the *ostR* ORF to generate strain BTH_I0021–153:ISlacZ-hah-Tc and T23 at position 89 of *emrB* (strain BTH_I0022–124::ISlacZ-PrhaBo-Tp/FRT). Transposon inserted mutants (Δ*ostR* and Δ*emrB*) were obtained from the Manoil laboratory and grown on LB-agar plates with 80 μg/ml tetracycline and 50 μg/ml trimethoprim, respectively (21). Single colonies were grown overnight after inoculating in LB medium with the respective antibiotics. To verify correct insertion of transposons, PCR was performed using primers BTH_21_Fw, BTH_22int_Fw, and LacZ_148 (Table S4).

Transposon insertion mutants Δ*emrB* and Δ*ostR* harbor trimethoprim and tetracycline antibiotic cassettes, respectively. Plasmids pFLPe4 or pCRE3 (a generous gift from H. Schweizer) were used to remove the antibiotic resistance cassettes from Δ*emrB* or Δ*ostR*, respectively (36, 37). In brief, Flp/Cre recombinase-encoding pFLPe4 or pCRE3 plasmid was transformed into *E. coli* TOP10 cells. Tri-parental mating was performed to transfer plasmids harboring Flp/Cre recombinase into Δ*emrB*

or Δ*ostR* stains, respectively. Selection was done on LSLB/kanamycin (for pFlpe4) or LSLB/ampicillin (for pCRE3) plates at 30 °C (where LSLB denotes low-salt LB). To induce *flp* or *cre* expression, selected colonies were streaked on LSLB/kanamycin/rhamnose (for pFlpe4) or LSLB/ampicillin/rhamnose (for pCRE3) plates. Corresponding antibiotic-sensitive clones were grown at 37 °C to induce loss of the temperature-sensitive pFlpe4/pCRE3. Removal of antibiotic cassettes was confirmed by PCR using primers (Tra_delE_Fw, Tra_delE_Rv; Cre_del21_Fw, Cre_del21_Rv; Table S4). Δ*emrB* and Δ*ostR* strains in which antibiotic resistance cassettes were removed were named Δ*emrBX* and Δ*ostRX*.

Genetic complementation

ostR with 170 bp upstream of the coding sequence was amplified using primers OstR_XbaI_Fw and OstR_KpnI_Rev (Table S4), which contain XbaI and KpnI sites, respectively. Digested PCR product was then cloned into the gentamicin-resistant broad host range cloning vector pBBR1-MCS5 (38). The construct was transformed into *E. coli* TOP10 (Invitrogen), and plasmid was verified by sequencing.

Tri-parental mating was performed to transfer plasmid harboring *ostR* to the *B. thailandensis* E264 Δ*ostR* strain. Conjugation was performed by mixing overnight cultures of donor (*E. coli* TOP10 containing pBBR1-MCS5 plasmid harboring *ostR*, grown in the presence of 80 μg/ml gentamicin), recipient (Δ*ostR* grown in the presence of 80 μg/ml tetracycline), and helper strain (HB101(pRK2013:Tn7)) in a ratio of 1:1:2. Residual antibiotics were removed by centrifuging the cells and washing pellets with 1.0 ml of LB four times. The pellets were then resuspended in 50 μl of LB and spotted on a preheated LB agar plate. After 12 h of incubation, cells were scraped off and resuspended in 1.0 ml of LB, and serial dilutions were spotted on LB-agar plates with 80 μg/ml tetracycline, 250 μg/ml gentamicin, and 8 μg/ml chloramphenicol. Individual colonies were screened to verify trans-conjugants by PCR with primers Con_pBBR_XbaI and Con_pBBR_KpnI (Table S4). The complemented strain is referred to as Δ*ostR*c. Empty plasmid pBBR1-MCS5 without the *ostR* gene was similarly transferred to WT *B. thailandensis*, and the strain was referred to as WTe.

Gene expression analysis

WT and mutant strains were grown overnight, followed by a 1:100 dilution of each culture in fresh LB media. Cultures were grown until A_{600} of ~0.5, and cells were harvested by centrifugation and washed with ice-cold diethyl pyrocarbonate–treated water. To determine the effect of oxidants (H_2O_2 or $CuCl_2$) and $ZnCl_2$ on gene expression, cells were grown until A_{600} of ~0.5 and treated with 2 mM H_2O_2, 2 mM $CuCl_2$, or 2 mM $ZnCl_2$ for 30 min, followed by harvesting and washing with diethyl pyrocarbonate–treated water. The effect of tetracycline on gene expression in Δ*ostRX* and Δ*emrBX* strains was determined after growing the cells overnight with tetracycline (5, 10, 20, 50, and 128 μg/ml). Cells were stored at −80 °C. The Illustra RNAspin Mini Isolation kit (GE Healthcare) was used to isolate total RNA. Any genomic DNA contamination was removed by Turbo DNase (Ambion) treatment, and PCR was performed using fresh RNA samples to verify the absence of genomic DNA. NanoDrop (Thermo Scientific) was used to measure the concentration of RNA. cDNA was prepared using gene-specific primers (Table S4) and 1 μg of RNA with 1 mM $MgCl_2$, 1 mM dNTP, 10 units of avian myeloblastosis virus reverse transcriptase (New England Biolabs) in 1× avian myeloblastosis virus reverse transcriptase buffer. The reaction mixture was incubated at 42 °C for 60 min. The qPCR was performed using a QuantStudio 6 Flex Real-Time PCR system and SYBR Green I (Sigma) to detect gene expression. Data were normalized to the reference gene glutamate synthase large subunit, which was amplified using primers GluSyn_qPCR_Fw and GluSyn_qPCR_Rv and expressed as $2^{-\Delta CT}$. The comparative C_T method ($2^{-\Delta\Delta CT}$) was used to analyze the effect of antibiotics, oxidants, and $ZnCl_2$ on gene expression. All expression analyses were performed in biological triplicates and are presented as mean ± S.D.

Plate assay and MIC determination

Sensitivity to antibiotics and oxidants was assessed by plate assays. Overnight cultures of WT and mutant strains were diluted 1:100 using LB medium and grown at 37 °C to A_{600} ~0.6. To assess the susceptibility to antibiotics, 5 μl of 10-fold serial dilutions were spotted on LB-agar plates containing the desired antibiotic (nalidixic acid, tetracycline, gentamicin, or trimethoprim). To determine the response to oxidants, 1 ml of each culture was incubated with 5 mM H_2O_2 or $CuCl_2$ for 30 min at 37 °C, followed by spotting 5 μl of 10-fold serial dilutions on LB-agar plates. Plates were incubated at 37 °C for 18–22 h.

MICs were estimated by preparing 2-fold dilutions of antibiotics in LB in 96-well microtiter plates. Overnight cultures were freshly diluted 1:100 in LB and grown to exponential phase; an equal volume of culture was added to the microtiter wells at an A_{600} of ~0.6. Cell growth was determined visually after incubation at 37 °C for 24 h.

Author contributions—A. S. and A. Grove conceptualization; A. S. formal analysis; A. S. and A. Grove validation; A. S., B. W. G., and A. Gupta investigation; A. S. visualization; A. S., A. Gupta, and A. Grove methodology; A. S. and A. Grove writing-original draft; A. S., A. Gupta, and A. Grove writing-review and editing; A. Grove supervision; A. Grove funding acquisition.

Acknowledgments—We thank H. Schweizer (University of Florida), for providing plasmids pFLPe4 and pCRE3, Z. Stewart for participation at early stages of this project, and M. Newcomer for use of the Nanodrop.

References

1. Deochand, D. K., and Grove, A. (2017) MarR family transcription factors: dynamic variations on a common scaffold. *Crit. Rev. Biochem. Mol. Biol.* **52,** 595–613 CrossRef Medline
2. Cohen, S. P., Levy, S. B., Foulds, J., and Rosner, J. L. (1993) Salicylate induction of antibiotic resistance in *Escherichia coli*: activation of the *mar* operon and a *mar*-independent pathway. *J. Bacteriol.* **175,** 7856–7862 CrossRef Medline
3. Rhodes, K. A., and Schweizer, H. P. (2016) Antibiotic resistance in *Burkholderia* species. *Drug Resist. Updat.* **28,** 82–90 CrossRef Medline
4. Piddock, L. J. (2006) Multidrug-resistance efflux pumps: not just for resistance. *Nat. Rev. Microbiol.* **4,** 629–636 CrossRef Medline

5. Saier, M. H., Jr. (2016) Transport protein evolution deduced from analysis of sequence, topology and structure. *Curr. Opin. Struct. Biol.* **38,** 9–17 CrossRef Medline
6. Titball, R. W., Burtnick, M. N., Bancroft, G. J., and Brett, P. (2017) *Burkholderia pseudomallei* and *Burkholderia mallei* vaccines: are we close to clinical trials? *Vaccine* **35,** 5981–5989 CrossRef Medline
7. Scoffone, V. C., Chiarelli, L. R., Trespidi, G., Mentasti, M., Riccardi, G., and Buroni, S. (2017) *Burkholderia cenocepacia* infections in cystic fibrosis patients: drug resistance and therapeutic approaches. *Front. Microbiol.* **8,** 1592 CrossRef Medline
8. Yu, Y., Kim, H. S., Chua, H. H., Lin, C. H., Sim, S. H., Lin, D., Derr, A., Engels, R., DeShazer, D., Birren, B., Nierman, W. C., and Tan, P. (2006) Genomic patterns of pathogen evolution revealed by comparison of *Burkholderia pseudomallei*, the causative agent of melioidosis, to avirulent *Burkholderia thailandensis*. *BMC Microbiol.* **6,** 46 CrossRef Medline
9. Sahl, J. W., Vazquez, A. J., Hall, C. M., Busch, J. D., Tuanyok, A., Mayo, M., Schupp, J. M., Lummis, M., Pearson, T., Shippy, K., Colman, R. E., Allender, C. J., Theobald, V., Sarovich, D. S., Price, E. P., *et al.* (2016) The effects of signal erosion and core genome reduction on the identification of diagnostic markers. *MBio* **7,** e00846-16 CrossRef Medline
10. Haraga, A., West, T. E., Brittnacher, M. J., Skerrett, S. J., and Miller, S. I. (2008) *Burkholderia thailandensis* as a model system for the study of the virulence-associated type III secretion system of *Burkholderia pseudomallei*. *Infect. Immun.* **76,** 5402–5411 CrossRef Medline
11. Fang, F. C. (2011) Antimicrobial actions of reactive oxygen species. *MBio* **2,** e00141-11 CrossRef Medline
12. Keyer, K., Gort, A. S., and Imlay, J. A. (1995) Superoxide and the production of oxidative DNA damage. *J. Bacteriol.* **177,** 6782–6790 CrossRef Medline
13. Imlay, J. A. (2013) The molecular mechanisms and physiological consequences of oxidative stress: lessons from a model bacterium. *Nat. Rev. Microbiol.* **11,** 443–454 CrossRef Medline
14. Lemire, J. A., Harrison, J. J., and Turner, R. J. (2013) Antimicrobial activity of metals: mechanisms, molecular targets and applications. *Nat. Rev. Microbiol.* **11,** 371–384 CrossRef Medline
15. Gupta, A., Fuentes, S. M., and Grove, A. (2017) Redox-sensitive MarR homologue BifR from *Burkholderia thailandensis* regulates biofilm formation. *Biochemistry* **56,** 2315–2327 CrossRef Medline
16. Pande, A., Veale, T. C., and Grove, A. (2018) Gene regulation by redox-sensitive *Burkholderia thailandensis* OhrR and its role in bacterial killing of *Caenorhabditis elegans*. *Infect. Immun.* **86,** e00322-00318 CrossRef Medline
17. Antelmann, H., and Helmann, J. D. (2011) Thiol-based redox switches and gene regulation. *Antioxid. Redox Signal.* **14,** 1049–1063 CrossRef Medline
18. Hao, Z., Lou, H., Zhu, R., Zhu, J., Zhang, D., Zhao, B. S., Zeng, S., Chen, X., Chan, J., He, C., and Chen, P. R. (2014) The multiple antibiotic resistance regulator MarR is a copper sensor in *Escherichia coli*. *Nat. Chem. Biol.* **10,** 21–28 CrossRef Medline
19. Gupta, A., Pande, A., Sabrin, A., Thapa, S. S., Gioe, B. W., and Grove, A. (2019) MarR family transcription factors from *Burkholderia* species: hidden clues to control of virulence-associated genes. *Microbiol. Mol. Biol. Rev.* **83,** e00039-18 CrossRef Medline
20. Quade, N., Mendonca, C., Herbst, K., Heroven, A. K., Ritter, C., Heinz, D. W., and Dersch, P. (2012) Structural basis for intrinsic thermosensing by the master virulence regulator RovA of *Yersinia*. *J. Biol. Chem.* **287,** 35796–35803 CrossRef Medline
21. Gallagher, L. A., Ramage, E., Patrapuvich, R., Weiss, E., Brittnacher, M., and Manoil, C. (2013) Sequence-defined transposon mutant library of *Burkholderia thailandensis*. *MBio* **4,** e00604-13 CrossRef Medline
22. Wigfield, S. M., Rigg, G. P., Kavari, M., Webb, A. K., Matthews, R. C., and Burnie, J. P. (2002) Identification of an immunodominant drug efflux pump in *Burkholderia cepacia*. *J. Antimicrob. Chemother.* **49,** 619–624 CrossRef Medline
23. Biot, F. V., Lopez, M. M., Poyot, T., Neulat-Ripoll, F., Lignon, S., Caclard, A., Thibault, F. M., Peinnequin, A., Pagès, J. M., and Valade, E. (2013) Interplay between three RND efflux pumps in doxycycline-selected strains of *Burkholderia thailandensis*. *PLoS One* **8,** e84068 CrossRef Medline
24. Bordelon, T., Wilkinson, S. P., Grove, A., and Newcomer, M. E. (2006) The crystal structure of the transcriptional regulator HucR from *Deinococcus radiodurans* reveals a repressor preconfigured for DNA binding. *J. Mol. Biol.* **360,** 168–177 CrossRef Medline
25. Deochand, D. K., Perera, I. C., Crochet, R. B., Gilbert, N. C., Newcomer, M. E., and Grove, A. (2016) Histidine switch controlling pH-dependent protein folding and DNA binding in a transcription factor at the core of synthetic network devices. *Mol. Biosyst.* **12,** 2417–2426 CrossRef Medline
26. Jones, D. T., and Cozzetto, D. (2015) DISOPRED3: precise disordered region predictions with annotated protein-binding activity. *Bioinformatics* **31,** 857–863 CrossRef Medline
27. Kushwaha, A. K., Deochand, D. K., and Grove, A. (2015) A moonlighting function of *Mycobacterium smegmatis* Ku in zinc homeostasis? *Protein Sci.* **24,** 253–263 CrossRef Medline
28. Kumar, A., Chua, K. L., and Schweizer, H. P. (2006) Method for regulated expression of single-copy efflux pump genes in a surrogate *Pseudomonas aeruginosa* strain: identification of the BpeEF-OprC chloramphenicol and trimethoprim efflux pump of *Burkholderia pseudomallei* 1026b. *Antimicrob. Agents Chemother.* **50,** 3460–3463 CrossRef Medline
29. Palm, G. J., Khanh Chi, B., Waack, P., Gronau, K., Becher, D., Albrecht, D., Hinrichs, W., Read, R. J., and Antelmann, H. (2012) Structural insights into the redox-switch mechanism of the MarR/DUF24-type regulator HypR. *Nucleic Acids Res.* **40,** 4178–4192 CrossRef Medline
30. Deochand, D. K., Meariman, J. K., and Grove, A. (2016) pH-dependent DNA distortion and repression of gene expression by *Pectobacterium atrosepticum* PecS. *ACS Chem. Biol.* **11,** 2049–2056 CrossRef Medline
31. Poole, L. B. (2015) The basics of thiols and cysteines in redox biology and chemistry. *Free Radic. Biol. Med.* **80,** 148–157 CrossRef Medline
32. Gupta, A., and Grove, A. (2014) Ligand-binding pocket bridges DNA-binding and dimerization domains of the urate-responsive MarR homologue MftR from *Burkholderia thailandensis*. *Biochemistry* **53,** 4368–4380 CrossRef Medline
33. Micsonai, A., Wien, F., Kernya, L., Lee, Y. H., Goto, Y., Réfrégiers, M., and Kardos, J. (2015) Accurate secondary structure prediction and fold recognition for circular dichroism spectroscopy. *Proc. Natl. Acad. Sci. U.S.A.* **112,** E3095–E3103 CrossRef Medline
34. Whitmore, L., and Wallace, B. A. (2004) DICHROWEB, an online server for protein secondary structure analyses from circular dichroism spectroscopic data. *Nucleic Acids Res.* **32,** W668–W673 CrossRef Medline
35. Whitmore, L., and Wallace, B. A. (2008) Protein secondary structure analyses from circular dichroism spectroscopy: methods and reference databases. *Biopolymers* **89,** 392–400 CrossRef Medline
36. Choi, K. H., Mima, T., Casart, Y., Rholl, D., Kumar, A., Beacham, I. R., and Schweizer, H. P. (2008) Genetic tools for select-agent-compliant manipulation of *Burkholderia pseudomallei*. *Appl. Environ. Microbiol.* **74,** 1064–1075 CrossRef Medline
37. Garcia, E. C. (2017) *Burkholderia thailandensis*: genetic manipulation. *Curr. Protoc. Microbiol.* **45,** 4C.2.1–4C.2.15 CrossRef Medline
38. Kovach, M. E., Elzer, P. H., Hill, D. S., Robertson, G. T., Farris, M. A., Roop, R. M., 2nd, and Peterson, K. M. (1995) Four new derivatives of the broad-host-range cloning vector pBBR1MCS, carrying different antibiotic-resistance cassettes. *Gene* **166,** 175–176 CrossRef Medline